Asymmetric Rowland Circle Geometries for Spherically Bent Crystal Analyzers in Laboratory and Synchrotron Applications

Journal:	*Journal of Analytical Atomic Spectrometry*
Manuscript ID	JA-ART-12-2023-000437.R1
Article Type:	Paper
Date Submitted by the Author:	22-Feb-2024
Complete List of Authors:	Gironda, Anthony; University of Washington, Materials Science and Engineering Abramson, Jared; University of Washington, Physics Chen, Yue; University of Washington, Physics Solovyev, Mikhail; Argonne National Laboratory Advanced Photon Source Sterbinsky, George; Argonne National Laboratory Seidler, Gerald; University of Washington, Physics

Asymmetric Rowland Circle Geometries for Spherically Bent Crystal Analyzers in Laboratory and Synchrotron Applications

Anthony J. Gironda[1], Jared E. Abramson[2], Yeu Chen[2], Mikhail Solovyev[3], George E. Sterbinsky[3], Gerald T. Seidler[2,*]

[1] Department of Materials Science and Engineering, University of Washington, Seattle WA
[2] Department of Physics, University of Washington, Seattle WA
[3] X-ray Science Division, Advanced Photon Source, Argonne National Laboratory, IL
*Corresponding author, seidler@uw.edu

Spherically bent crystal analyzers (SBCAs) are the dominant high-resolution hard x-ray optic in the ongoing rebirth of laboratory-based x-ray absorption fine structure (XAFS) and x-ray emission spectroscopy (XES) as well as in synchrotron methods such as high energy resolution fluorescence detection (HERFD) and non-resonant x-ray Raman scattering (XRS). In the overwhelming majority of cases, SBCAs are implemented in a 'symmetric' configuration on the Rowland circle, wherein the diffracting crystal plane is nominally coincident with the analyzer surface. We report here comprehensive investigations of 'asymmetric' operation of SBCA on the Rowland circle, wherein the diffracting crystal plane is not coincident with the optical surface of the analyzer. First, we have developed a laboratory spectrometer for XAFS and XES that is specialized for asymmetric SBCA operation. We find several benefits, including the capacity to use a single SBCA over a very wide energy range via '*hkl* hopping' and the frequent ability to eliminate Johann error, the most prevalent energy-broadening mechanism when using SBCA symmetrically on the Rowland circle. Second, we expand these ideas to synchrotron facilities with a demonstration study of HERFD and XRS where asymmetric operation also provided advantage. Our results suggest that large-array systems for HERFD augmented with an additional mechanical degree of freedom could streamline user operation and also indicate benefits to XRS in the asymmetric configuration, where larger solid angle, larger sample-to-detector distance, and decreased Johann error can be achieved simultaneously.

1. Introduction

Spherically bent crystal analyzers (SBCAs), specifically those with Johann-type profiles[1], are hard x-ray optics that provide a useful combination of large collection solid angle and fine energy resolution. This has resulted in their extensive use in the ongoing rebirth of laboratory-based x-ray absorption fine structure (XAFS) and x-ray emission spectroscopy (XES)[2–10] in addition to their historical and continued use as workhorse optics for high-resolution photon-in photon-out x-ray spectroscopy at synchrotron facilities.[11–18] With infrequent but valuable exceptions[19–22], such applications have been in a 'symmetric' Rowland circle configuration wherein the diffracting plane is nominally coincident with the surface of the SBCA diffracting wafer.

Here, we propose that asymmetric operation of SBCA on the Rowland circle is an underutilized opportunity. The basic parameters for asymmetric Rowland circle operation are defined in Fig. 1. In the Figure, note the asymmetry angle α, the need for a 'mechanical' analyzer angle θ_M, and the inequality of the chord lengths ρ and *d* when $\alpha \neq 0$. The usual theorem for equality of inscribed angles still holds when $\alpha \neq 0$ so that the optic still functions as

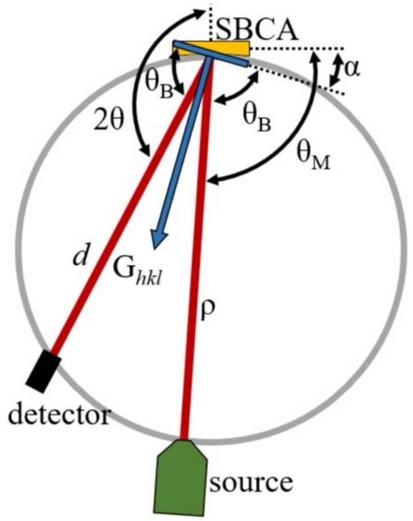

Figure 1: Diagram of spectrometer components during asymmetric operation in the reference frame of the SBCA. α denotes the angle between the diffracting plane for the reflection $\mathbf{G}_{hkl}$ and the plane at the optic's surface (nominally normal to the reciprocal lattice vector $\mathbf{G}_0$). Note the chord lengths *d* and ρ differ when $\alpha \neq 0$.

a monochromator in the Rowland plane, barring Johann error which will be discussed in detail later. Out-of-plane astigmatism at large α can become considerable, but we find that is not a significant limitation on energy resolution. It is not difficult to derive the dependence of the parameters in Fig. 1 on the Bragg angle, θ_B, and α, specifically

$$\begin{aligned} \rho &= D\sin(\theta_B + \alpha) \\ d &= D\sin(\theta_B - \alpha) \qquad \text{Eqs. (1)} \\ 2\theta &= 2\theta_B \\ \theta_M &= \theta_B + \alpha \end{aligned}$$

where *D* is the diameter of the Rowland circle or equivalently the radius of curvature of the Johann SBCA.

With this background established, we address the potential advantages of asymmetric operation as a central principle in spectrometer design. We denote by $\mathbf{G}_0$ the reciprocal lattice vector normal to the wafer surface and assume the wafer miscut is small. Choosing $\mathbf{G}_0$ is equivalent to choosing which wafer material and orientation to use in the optic, and it determines the useful energy range in symmetric operation -- Bragg angles below 60 deg generally suffer degraded energy resolution due to Johann error and source-size broadening. While analyzer harmonics sometimes enable high-resolution access to a few distinct energy ranges[23], both laboratory instruments and synchrotron facilities typically fabricate or acquire a suite of SBCAs having a variety of $\mathbf{G}_0$ vectors.

Asymmetric operation modifies these considerations. Any single crystal has a multitude of additional crystal planes at various angles to the surface. Each allowed reflection capable of diffraction in an asymmetric configuration gives an additional useful energy range dependent on its own *d*-spacing. Hence, as a first advantage, we show below that asymmetric operation of a single SBCA can permit high-resolution performance for photon energies from 5 keV through 10 keV and beyond with no gaps in the energy range. The good performance of many different reflections of various Miller indices (*hkl*) from a single analyzer is a major result of the present study, and we find it appropriate to introduce the term '*hkl* hopping' when a monochromator jumps between different Miller indices of a single SBCA to adjust energy range or to improve energy resolution, which we now address.

The second advantage of asymmetric operation is the minimization or even elimination of Johann error for SBCAs; prior work by Suortti and others for curved analyzers on the Rowland circle as well as asymmetric applications in other fields and other classes of optics motivates and supports this inquiry[21,22,24–35]. Briefly, Johann analyzers possess a radius of curvature for the diffracting wafer that is equal to the diameter of the desired Rowland circle. This yields the necessary suface orientations but results in small displacements between the wafer surface and the Rowland circle at the analyzer edges with corresponding errors in the Bragg angle upon moving away from the analyzer center. There is consequently a characteristic low energy tail in the analyzer's energy response function[36].

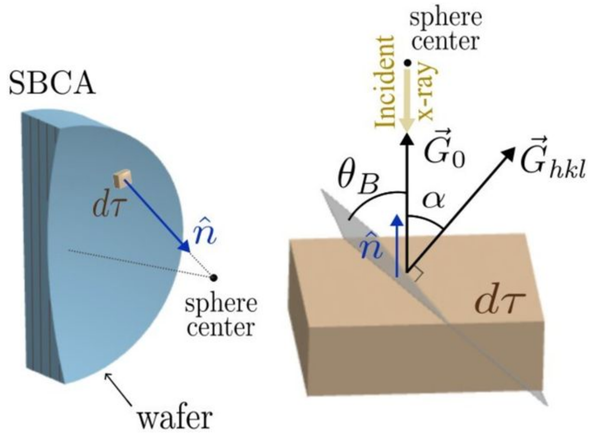

Figure 2: An infinitesimal single crystal element (right) of a spherically bent crystal analyzer (left), demonstrating a geometric argument for the elimination of Johann error in asymmetric Rowland geometries when the source is close to the sphere-center of the SBCA curved wafer.

The underlying principle for suppression of Johann error via asymmetric operation is illustrated in Fig. 2. As shown, consider the special case where all incident x-rays have an incoming path exactly normal to each infinitesimal crystallite that makes up the SBCA surface, i.e., the special case where a point source is located at the sphere center of the curved analyzer wafer surface. The key observation is that for every point on the analyzer surface, the angle between an arbitarily chosen reciprocal lattice vector $\mathbf{G}_{hkl}$ and the incident x-ray is the same everywhere on the surface. Hence, in this special case the Bragg angle is the same at every point on the surface and Johann error from the lack of coincidence between the edges of the analyzer and the Rowland circle is eliminated. More generally, asymmetric operation allows operation with the source *closer to* the sphere center than is often possible symmtrically, and hence with dereased Johann error. We illustrate this later with XANES and XES measurements.

Finally, a third benefit comes from those special geometries that are expected to fully eliminate Johann error, as described by Fig. 2. Non-resonant x-ray Raman scattering (XRS), i.e., the non-resonant inelastic x-ray scattering from semicore levels, gives a hard x-ray analog to electron energy loss spectroscopy and allows x-ray spectroscopy on low-energy shells while using high-energy photons. This capability has seen sufficient demand that several dedicated facilities have been constructed at synchrotron facilities[37–41]. However, the extremely small cross-section for inelastic scattering from the semicore levels makes all XRS spectrometers subject to severe competition between the collection solid angle and the energy resolution. The best practice to date has been to use banks of 1-m SBCA as close as possible to a backscatter geometry in symmetric Rowland operation, together with considerable diligence to reject background scatter[12,14,17,18]. That being said, achieving highest energy resolution still requires analyzer masking to reduce Johann error; in some cases, small off-circle broadening is accepted as a compromise that aids with clearance between detector and the beam spot on the sample[13]. The more recently available 0.5-m SBCA having four times the solid angle of the older 1-m SBCA have not been used for XRS because their larger angular size results in far larger Johann error *in symmetric operation*. On the other hand, the Johann-rejection strategy of Fig. 2 provides a possible path toward simultaneously attaining large solid angle, fine energy resolution, and large clearance between sample and detector. XRS measurements are performed in so-called inverse-scanning mode where a single energy is chosen for the outgoing (analyzed) photon while the incident monochromator is scanned to create the necessary range of energy losses: *the spectrometer must have low Johann error at only a single energy*.

In this paper we address all three of these proposed benefits. We describe a new laboratory-based XAFS and XES hard x-ray spectrometer specifically designed to enable easy exploration of asymmetric Rowland geometries. With this instrument we demonstrate *hkl* hopping over a broad energy range and also demonstrate the minimization of Johann error through choice of the favorable special geometry with the source near the spherical center of the analyzer. These benefits also appear in our preliminary synchrotron studies, where we use asymmetric reflections to access the otherwise inconvenient Zn Kα_1 for high-energy resolution fluorescence detection (HERFD) x-ray absorption spectroscopy and also use an optimal asymmetric configuration for XRS via an 0.5-m radius SBCA. This ensemble of results across laboratory and synchrotron venues supports the hypothesis that asymmetric operation of SBCA has been underutilized and suggests directions for further inquiry.

II. Laboratory Spectrometer Design and Operation

We now present the six main spectrometer systems in order: the x-ray enclosure, x-ray sources, the detector and its subassembly, the optic, the motorization of the primary Rowland circle degrees of freedom, the additional motorized degree of freedom used to rotate many different desired reflections into the Rowland plane, and the overall control software.

The spectrometer is housed in a steel enclosure, approximately 1.8-m wide by 1.5-m deep by 1.3-m tall. The slightly oversized enclosure provides ample space for special sample environments in the future such as a cryostat or additional equipment such as a potentiostat for *operando* electrochemical measurements. The computer-aided design (CAD) rendering in Fig. 3 shows the design of the spectrometer and its key components in Rowland circle geometries configured for XAFS and XES measurements in Fig. 3 (a) and (b), respectively. In XAFS mode (Fig. 3 (a)), a 100 W X-ray source (Varex VF-80 Pd-anode tube) with variable width entrance slits to adjust apparent source size is placed on-circle via manual slide. In XES mode (Fig. 3 (b)), a 3 kW X-ray source (Varex OEG-76H W-anode tube) with a preliminary 1 mm fixed-width entrance slit on the sample enclosure is placed on-circle via manual slide. A kinematic feature at the fixed source location ensures precise placement of radiation entrance slits on circle. A 100 W x-ray tube with a tungsten anode, but otherwise identical to the XAFS-mode source, was used for commissioning in XES measurements (not shown in the figure).

The detector is a silicon drift detector (SDD) with 150 mm^2 area sensing element (KETEK AXAS M-1) mounted on a motorized linear stage (Velmex XSlide) to adjust the detector-analyzer chord length. The optics are 0.5-m radius of curvature SBCAs (XRS Tech). The chord lengths and angular positioning of the detector and optic are motorized. The optic and detector subassemblies are concentrically mounted on the θ and 2θ rotation stages, respectively, of a repurposed goniometer from a commercial X-ray diffraction instrument (Bruker D8 Advance). The θ and 2θ stages of the goniometer are independent, allowing for the α offsets required in asymmetric operation. The entire goniometer-detector-optic subassembly is mounted on a motorized linear stage (Velmex tandem BiSlide) to adjust source-analyzer chord length, ρ.

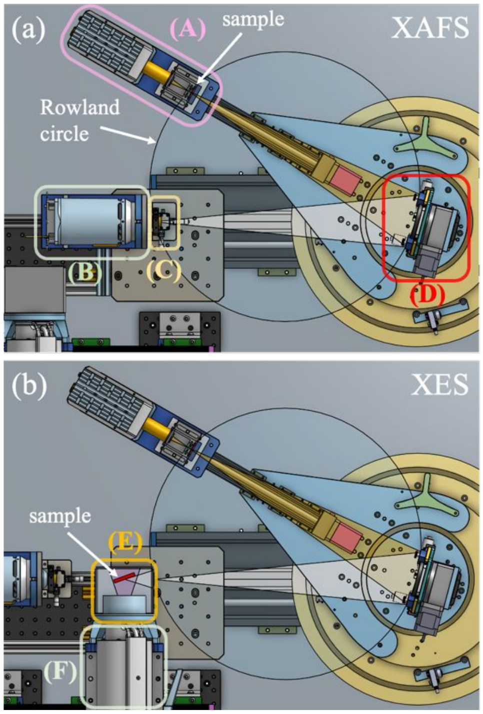

Figure 3: Top-view CAD renderings of the spectrometer configured for **(a)** XAFS and **(b)** XES measurements. The key components are outlined with boxes and labelled as follows: (A) detector, (B) 100 W XAFS source, (C) Adjustable-width XAFS entrance slit, (D) crystal analyzer and optic tower, (E) XES sample enclosure and entrance slit, and (F) 3 kW XES source.

For automated asymmetric operation, an additional motorized degree of freedom we refer to as the ‘clock angle’ or φ is required in the optic subassembly. This additional degree of freedom also enables motorized tilt-free correction of crystal miscut.[42] CAD renderings of the optic cartridge, the full optic tower assembly, and the φ rotation stage and direction are shown in the three panels of Fig. 4. The cartridge mounts concentrically on a small, motorized rotation stage (Velmex B5990TS). The fine adjustment *x*-*y* stage at the base of the optic tower aligned the optic on the rotation axis of the goniometer during spectrometer commissioning.

Recalling from the introduction the requirements for asymmetric Rowland configurations, the spectrometer achieves these geometries by using independent rotation and linear stages. Representative symmetric and asymmetric configurations are shown in CAD renderings in Fig. 5. Specifically, Fig. 5(a) shows a typical symmetric operation at an unfavorable θ_B far from backscatter, whereas Fig. 5(b) shows an asymmetric configuration at the same θ_B but satisfying the condition of $\theta_B + \alpha = 90$ deg, the configuration that is expected to eliminate Johann error, recall Fig. 2. It is important to note Fig. 5(a) and (b) could be at radically different energies because of the different *d*-spacings for $\mathbf{G}_0$ and $\mathbf{G}_{hkl}$. The purpose of the Figure is to demonstrate the difference in geometries in these different diffracting conditions. Note that the chord lengths between source-and-analyzer and analyzer-and-detector become unequal when $\alpha \neq 0$.

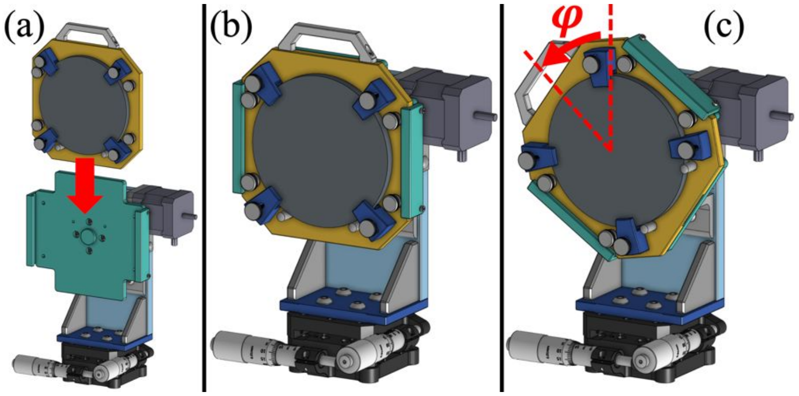

Figure 4: **(a)** An optic cartridge is loaded into the optic tower subassembly. **(b)** The fully assembled motorized optic tower which concentrically indexes the crystal on a motorized rotation stage. **(c)** The motorized azimuthal (φ) degree of freedom allows for tilt-free correction of crystal miscut and for automated asymmetric operation.

The spectrometer control software consists of two main components. First, a library of routines was written in Python (Jupyter) to generate ASCII files with component-by-component instructions for each step in any desired spectrometer scan. Second, LabView software was written to interpret the scan definition files and execute the desired measurements by commanding the motors and reading the detector. The LabView software can define measurement projects that perform sequences of measurements each parametrized by a different scan definition file including for successive scans using different $\mathbf{G}_{hkl}$. For both XAFS and XES, the energy is scanned by stepping the crystal angle $\theta_M$and satisfying the Rowland circle geometry at a particular Bragg angle by driving the ρ, detector, and 2θ stages.

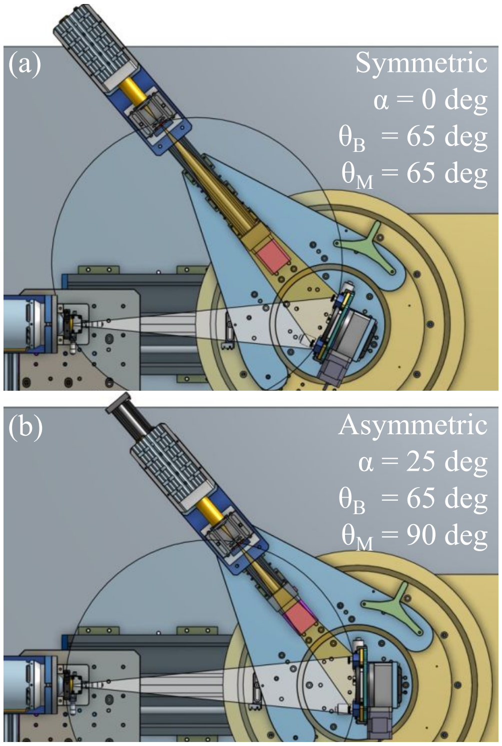

Figure 5: **(a)** Symmetric spectrometer operation at $\theta_B = 65$ deg in XAFS mode. **(b)** Asymmetric spectrometer operation at the same θ_B with $\alpha = 25$ deg, placing the source diametrically from the optic resulting in a monochromatic diffracted beam with no Johann broadening.

III. Methods

Ray tracing simulations are generated using the xrt Python package[43]. The ray tracing calculations use a 250-μm by 250-μm area source and a 100-mm diameter, 0.5-m SBCA in both symmetric and asymmetric Rowland circle configurations, thus approximating the experimental conditions. Calculations for the location of asymmetric reflections and their resulting energy ranges were performed in home-written software in Python (Jupyter).

XES and XAFS measurements were taken with the laboratory-based instrument described in Section II using only a 100 W source in both configurations. Studies were selected to demonstrate instrument capabilities to characterize the advantages of asymmetric operation. For XAFS, standard metal reference foils of Cu and Ni (EXAFS Materials) were used. To demonstrate the extended energy range afforded by asymmetric operation, a multi-component transition metal oxide sample was prepared for XES. Equal masses of V_2O_3, MnO, FeO, NiO, CuO, ZnO, and $SrTiO_3$ were dry milled together to homogeneously mix the sample. The multi-component powder was enclosed in a polyimide pouch for XES study.

XRS and HERFD-XANES measurements were performed at sector 25-ID of the Advanced Photon Source. This used a Si(111) double crystal monochromator and a set of Kirkpatrick-Baez mirrors to achieve an approximately 100 μm by 100 μm spot size on the sample. The monochromator was not detuned, and the resulting expected energy resolution is 1.2 - 1.3 eV at 8700 eV. An Eiger S 500K camera (Dectris Corp.) was used to measure the x-rays analyzed by the SBCA (XRS Tech) and an SDD (Hitachi, Vortex) was used to measure total fluorescence yield in the HERFD study. The HERFD sample was a ZnO film with embedded Ge nanocrystals, prepared by sequential sputtering of ZnO and Ge targets under reactive ZnO growth conditions[44]. The XRS sample was an 0.9-mm diameter cylinder of randomly oriented graphite in a low-Z binder (mechanical pencil lead). For both studies the incident flux was $\sim 3 \times 10^{12}$ ph/sec.

IV. Results and Discussion

IV.A. The Asymmetric Rowland Geometry in the Laboratory

We begin by illustrating a central motivation of asymmetric operation, i.e., the large number of crystal planes that are available and the consequently wide energy range that can be accessed with fine energy resolution for a single SBCA. See Fig. 6. In panel (a) we show the calculated locations for a large number of asymmetric reflections for a Si(551) analyzer in terms of the asymmetry angle α (radial direction in the polar plot) and the clock angle φ (azimuthal direction in the polar plot). Note that the $\mathbf{G}_0$=(551) reflection itself is at the center of the polar plot. In panel (b) we show an experimental survey of the (α, φ) space at θ_B= 82 deg and find excellent agreement with the calculations of panel (a). In addition, as shown by the color scale indicating the dominant energy detected at a given location, we observe that a very large energy range can likely be patched together by *hkl*-hopping between different asymmetric configurations. This type of study is readily performed in the laboratory because of the very broad bremsstrahlung spectrum of x-ray tubes. Panels (c) and (d) show analogous calculations and experimental results for a Si(221) analyzer. Miller indices in panels (b) and (d) were identified by consistency between the theoretical (α, φ) polar plot with all allowed reflections and the results of converting the observed energy of an experimental reflection to the sum of squared indices by Bragg's law.

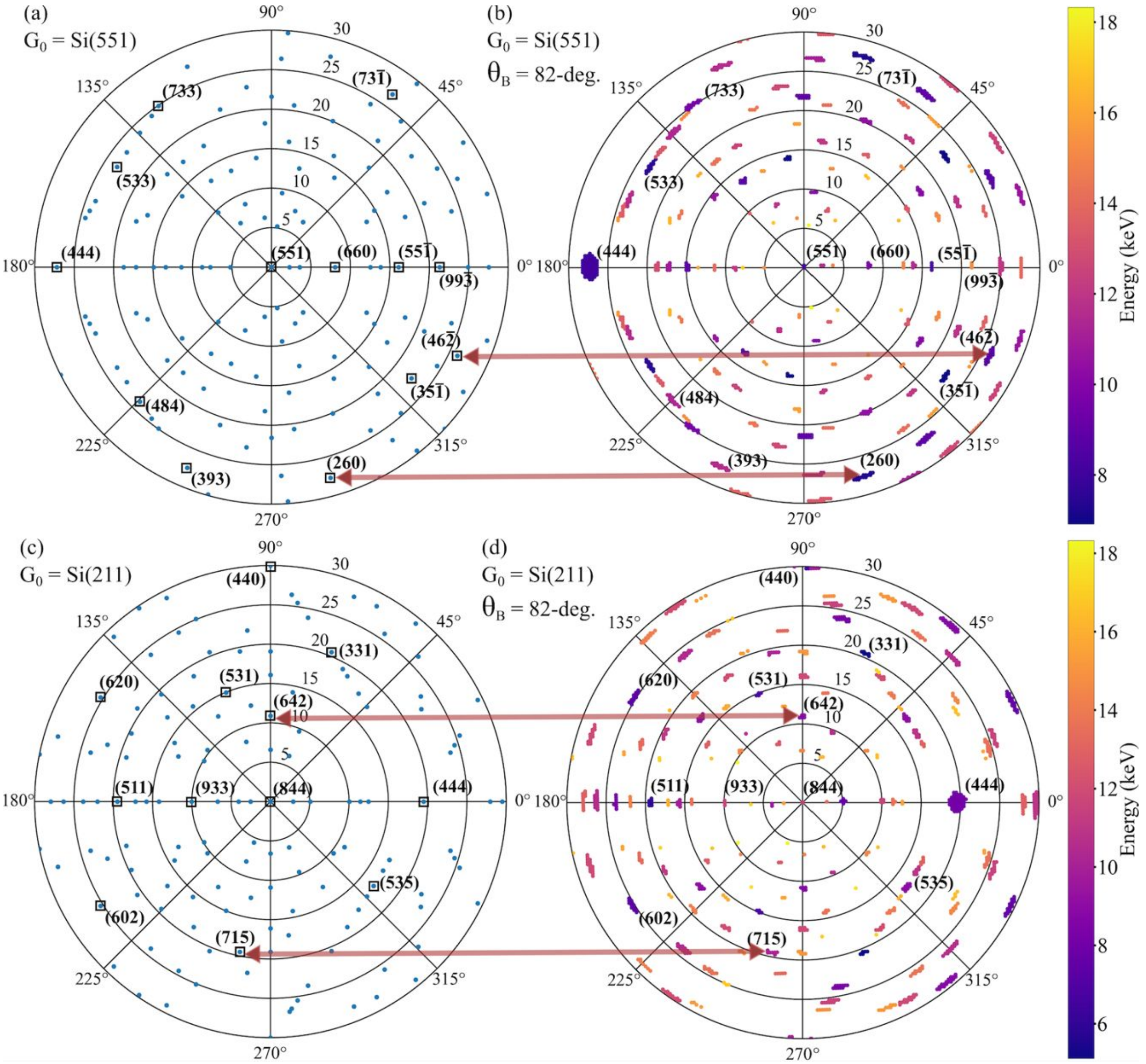

Figure 6: Polar plots in (α, ϕ) for calculated and measured reflections. (a) Calculated values of selected asymmetric reflections of a Si(551) analyzer. (b) Experimental data for Si(551) SBCA obtained by sampling phi-alpha space values at a fixed Bragg angle. (c) Calculated values of asymmetric Si(211) reflections. (d) Experimental data for Si(211) SBCAs. A threshold on reflection intensity was implemented to remove background in experimental data.

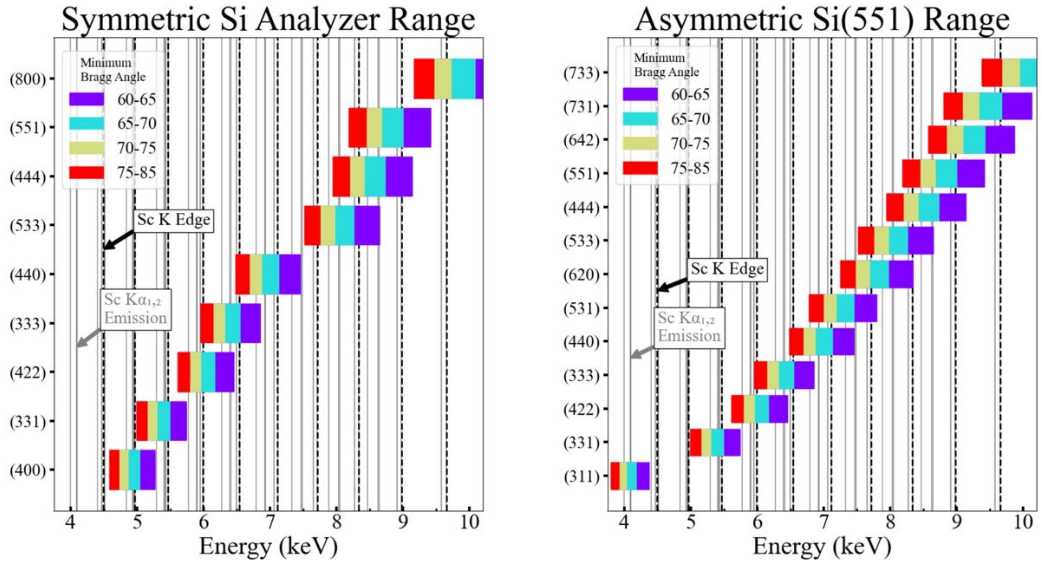

Figure 7: (Left) Diagram of the energy range achievable operating symmetrically with the Si SBCAs commonly used for transition metal XAS and XES: $\mathbf{G}_0$ = (100), (110), (111), (211), (331), (533), (551). The vertical gray lines indicate emission lines and the vertical black dashed lines indicate K-edges between 4 and 10 keV. (Right) Diagram of the energy range achievable operating asymmetrically with a Si(551) SBCA. Duplicate reflections, those that cover the exact same energy range at the same Bragg angle are omitted for clarity.

In both Fig. 6 (b) and (d) an azimuthal smearing is seen in the experimental results at large values of α near the borders of the pole plots. When at large asymmetries the chord length *d* from the SBCA to the detector becomes much smaller than the vertical radius of curvature of the analyzer, resulting in a significant vertical (perpendicular to the Rowland plane) extension and enlargement of the sagittal defocusing of the analyzed x-rays. The loss of intensity that occurs when the analyzed beam height is larger than the active diameter of the spectrometer's SDD is a confounding factor that leads to a trade-off between analyzed flux and the experimental convenience of asymmetric operation.

In Fig. 7 we compare the energy ranges of a conventional suite of SBCA operating symmetrically and the accessible diffraction planes of a single SBCA operated asymmetrically. This is investigated for the energy range of absorption edges and emission lines of the 3*d* transition metals. A comprehensive energy range is possible with a single analyzer operating asymmetrically and a suitable reflection is nearly always available that is close to the special condition (with the source moderately close to the analyzer spherical center) for a given emission or absorption edge. Hence, both a large energy range and high energy resolution should be expected with the Si(551) analyzer studied in the right panel of Fig. 7. We emphasize that there are complicated trade-offs between energy range coverage and analyzed flux (due to the vertical extent of the analyzed beam, described above), and we do not claim that Si(551) is necessarily optimal, although it does illustrate a favorable case for the argument being made here.

We next access a series of planes of the Si(551) SBCA on the amalgam XES, see Fig. 8. We measure Kα, Kβ, and valence-to-core (VTC) emission *en masse* with a single analyzer, demonstrating an expanded energy range through *hkl* hopping. The optimal reflections for the study are given in the left-hand side of Table 1; the experimental reflections used modestly differ in some cases. Fifteen emission lines spanning ~5 keV to ~14 keV were collected across seven elemental species using nine unique diffraction planes from the Si(551) analyzer. By comparison, under symmetric operation at useful Bragg angles the Si(551) crystal has an energy range of only ~8.2 – 9.3 keV and the same emission measurements would require a considerable number of separate Si optics, even if somewhat inferior Bragg angles were employed.

Table 1. Optimal asymmetric reflections for $\mathbf{G}_0$ = Si(551) and best symmetric counterparts for 3*d* transition metal XES, where both Si and Ge analyzers are considered for the symmetric case. For each emission line, the configuration expected to have the least Johann error is given in bold.

Emission	Energy (eV)	$\mathbf{G}_{hkl}$	θ_B (deg.)	α (deg.)	θ_M (deg.)	Best Si Symmetric Analyzer	θ_B (deg.)	Best Ge Symmetric Analyzer	θ_B (deg.)
V Kβ	5428	$(33\bar{1})$	66.47	21.31	**87.78**	(331)	66.47	(422)	81.49
Mn Kα	5900	(422)	71.44	23.84	**95.28**	(422)	71.44	(511) or (333)	74.81
Mn Kβ	6492	(333)	66.04	27.21	93.25	(440)	84.06	(531)	**86.94**
Fe Kα	6405	(333)	67.85	27.21	**95.06**	(511) or (333)	67.85	(440)	75.42
Fe Kβ	7059	(531)	73.11	13.97	**87.08**	(531)	73.11	(620)	79.04
Ni Kα	7480	(620)	74.87	27.67	**102.54**	(620)	74.87	(533)	73.87
Ni Kβ	8267	$(55\bar{1})$	80.49	16.1	**96.59**	(551) or (711)	80.49	(642)	82.7
Cu Kα	8046	(444)	79.45	27.21	106.66	(444)	**79.45**	(551) or (711)	76.55
Cu Kβ	8904	(731)	80.03	21.61	101.64	(731) or (553)	**80.03**	(800)	79.91
Zn Kα	8637	(642)	81.57	13.34	**94.91**	(642)	81.57	(553) or (731)	77.04
Zn Kβ	9570	(733)	77.56	24.95	102.51	(733)	77.56	(555) or (751)	**82.57**
Sr Kα	14,161	(884)	75.35	11.42	**86.77**	(777) or (11 5 1)	77.77	(991)	81.09
Sr Kβ	15,825	(12 6 2)	78.13	18.25	**96.38**	(13 3 3) or (995)	80.53	(13 5 3) or (11 9 1)	80.6

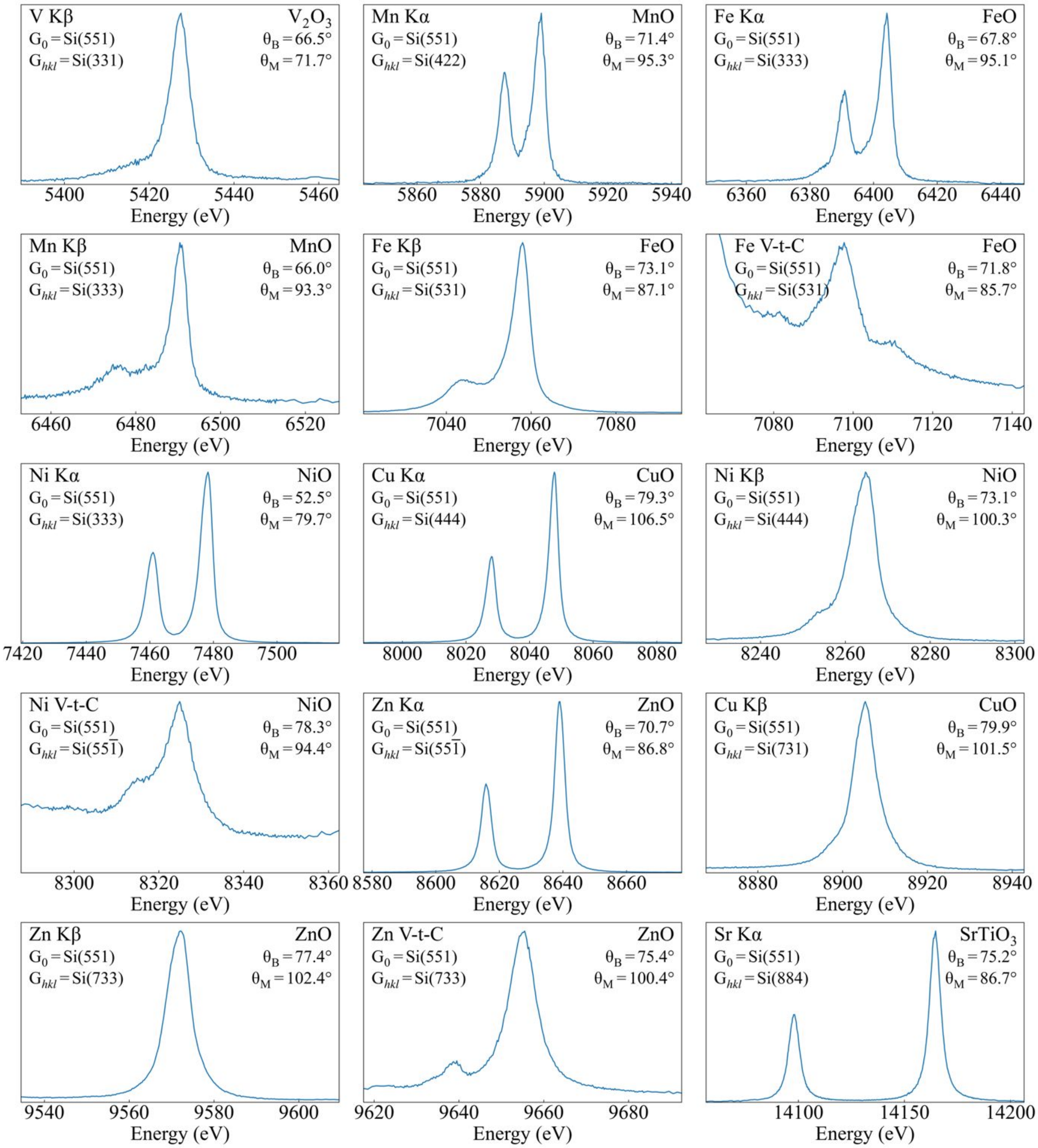

Figure 8: Emission lines measured asymmetrically with a Si(551) analyzer, arranged in order of ascending energy, presented with no background subtraction. The Bragg angle required to select the nominal energy of the emission line is given for each scan.

Having established the comprehensive advantage of a greatly increased energy range, we now address the proposed second benefit of asymmetric operation: an enhanced energy

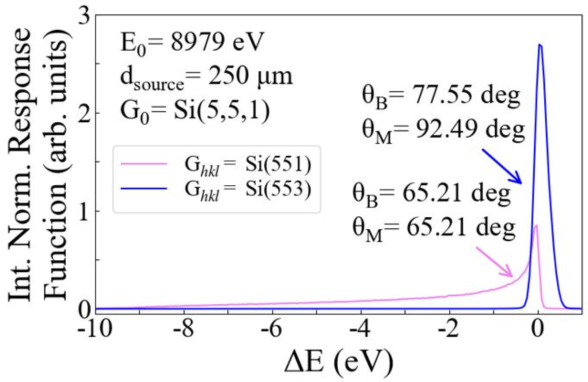

Figure 10: Symmetric and asymmetric energy response functions corresponding to Fig.9 (a) and (b), demonstrating the reduction of Johann error.

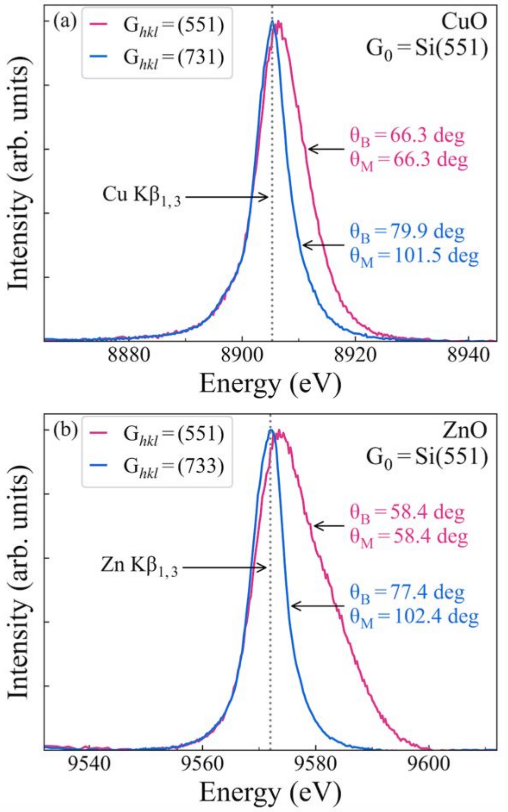

Figure 11: $K\beta_{1,3}$ emission spectra of (a) Cu and (b) Zn. Spectra were collected using the Si(551) SBCA symmetrically and with the most optimal asymmetric plane. Further from backscatter, the symmetric reflection analyzer response function broadens due to Johann error. On the other hand, the asymmetric reflection response function is narrow because of a mechanical analyzer angle, θ_M, close to 90 deg.

resolution compared to symmetric cases through elimination of Johann error when $\theta_B + \alpha = \theta_M \sim 90$ deg. Ray tracing simulations in Fig. 9 show the reduction of Johann error when approaching this special condition. Fig. 9 (a) shows an equatorial full-range broadening of ~9 eV at the analyzer edge of an SBCA at $\theta_B = 65$ deg. Fig. 9 (b), at the same photon energy, shows less than 10% as much broadening (with an opposite sign) for $\theta_B = 77.5$ deg and $\alpha = 14.9$ deg.

The ray tracing results show the availability of an asymmetric plane at the same energy as its conventional symmetric counterpart but with improved energy resolution via reduction of Johann broadening. This is further illustrated in Fig. 10, which shows the energy response functions corresponding to cases (a) and (b) of Fig. 9. The general consideration that Johann

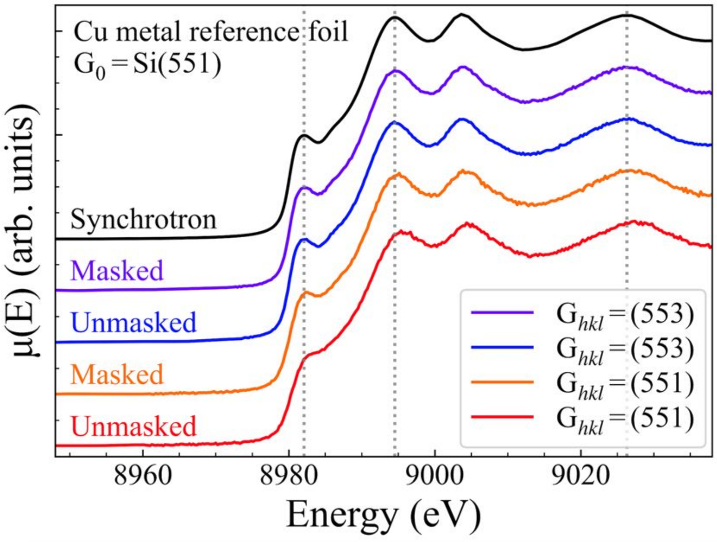

Figure 12: Cu K XANES measured using a Si(551) analyzer symmetrically and $\mathbf{G}_{hkl}$ = (553) reflection asymmetrically, compared to synchrotron results. At 8978.9 eV, $\theta_B = \theta_M = 65.2$ deg symmetrically whereas $\theta_B = 77.5$ and $\theta_M = 92.5$ deg. The asymmetric configuration eliminates Johann error by operating mechanically at near backscatter. Masking the edges of the analyzer removes Johann broadening in the symmetric case, whereas masking in the asymmetric case shows no appreciable difference in energy resolution. Spectra are offset for clarity of presentation.

error is smallest when the source is near to the SBCA sphere center is also investigated in Table 1, where the most favorable cases with respect to this condition are shown in bold for each emission line. The asymmetric option from even the single favorable case of a Si(551) analyzer are always quite close to the best choices among Si or Ge analyzers used symmetrically and is generally better by this metric.

To show this Johann error reduction in practice, Cu and Zn Kβ XES on the amalgam sample were measured using both (somewhat unfavorable) symmetric and (rather favorable) asymmetric configurations. Fig. 11(a) and (b) shows significant difference in the width and symmetry of the characteristic emission. The symmetric spectrum is broadened with a tail primarily because of Johann error, as well as some contribution from source size broadening. Asymmetric reflections with θ_M near backscatter have improved energy resolution through elimination of Johann error. The effect is more evident in Fig. 11(b) as the symmetric Zn measurement is far from backscatter at $\theta_B = 58$ deg, so broadening is more pronounced. The standard deviation of the energy response function calculated via ray tracing in the asymmetric case of the Zn measurement was 0.6 eV, compared to 4.6 eV in the symmetric case. The broadening in the asymmetric case is largely from source size effects.

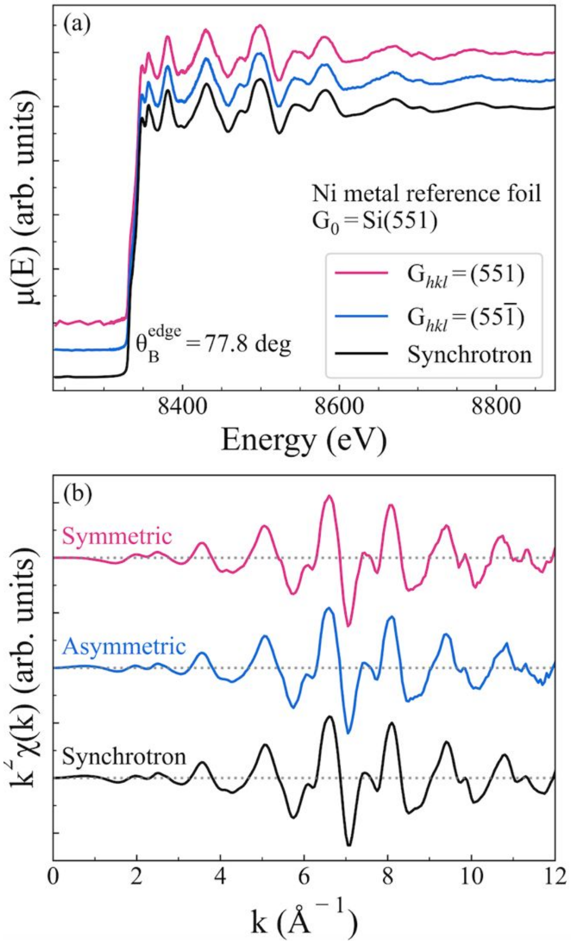

Figure 13: Ni K XAFS measured using a Si(551) analyzer symmetrically and with the $\mathbf{G}_{hkl} = (55\bar{1})$ reflection asymmetrically, compared to synchrotron results. Both spectra show agreement with synchrotron data. Spectra are offset for clarity of presentation.

To further investigate energy resolution effects, we performed transmission mode XANES and EXAFS studies on metal reference foils in symmetric and asymmetric SBCA configurations. Fig. 12 shows Cu XANES, selected for the well-known shoulder feature in its rising edge, measured symmetrically and asymmetrically with and without analyzer masking and compared to synchrotron data. Johann error both broadens and shifts the spectra, as shown in the unmasked symmetric case having $\theta_B = \theta_M = 65.2$ deg at the absorption edge, and analyzer masking improves the energy resolution of the symmetric data. However, the asymmetric spectra are unaffected by analyzer masking as Johann error is eliminated in the optical configuration with $\theta_B = 77.5$ and $\theta_M = 92.5$ deg, and the asymmetric spectra shows superb energy resolution with no loss of information compared to the synchrotron reference data.

Next, the Ni K-edge EXAFS was measured symmetrically and asymmetrically using the Si(551) analyzer and reflections $\mathbf{G}_0 = (551)$ and $\mathbf{G}_{hkl} = (55\bar{1})$ and compared to synchrotron data. The raw EXAFS and $\chi(k)$ are shown in Fig. 13 (a) and (b). There is again no loss in information between synchrotron and laboratory XAFS. The symmetric and asymmetric results are identical here because the Johann broadening in the symmetric case has little effect for spectrally broad features over the large energy range studied.

IV.B. Synchrotron Measurements

Having demonstrated some benefits of asymmetric Rowland geometry in laboratory x-ray spectroscopy, we extend the discussion to synchrotron x-ray measurements. Fig. 14 shows the asymmetric Rowland geometry of the monochromator for a HERFD-XANES measurement, tuned to the Zn Kα_1 emission energy for a study of a ZnO thin film. Note that while Si(642) is the preferred symmetric analyzer, it is an uncommon SBCA and in our case did not exist at any of the several beamlines performing XES or HERFD at our synchrotron, whereas the Si(211) is

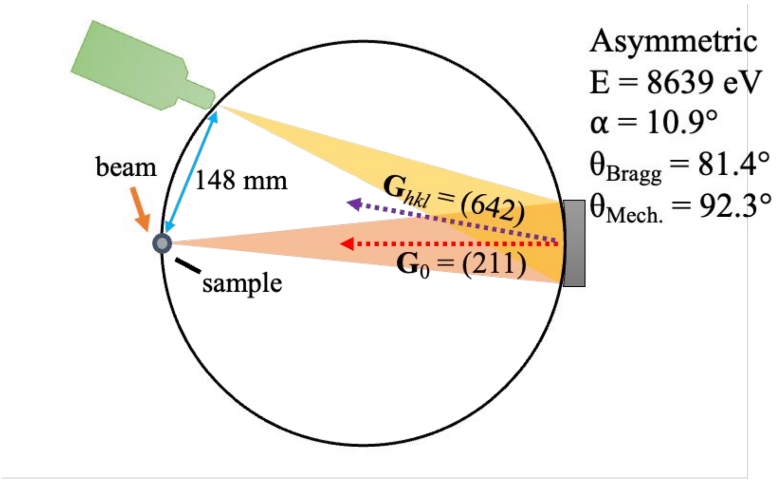

Figure 14: The asymmetric configuration implemented for HERFD-XANES measurements. Note the longer source-detector chord length (blue arrows), allowing greater flexibility in special sample environments and less size constraints than a symmetric counterpart.

relatively common for its (422) reflection to study XES for vanadium. Fig. 15 shows the HERFD-XANES collected using the asymmetric $\mathbf{G}_{hkl}$ = (642) reflection of a Si(211) SBCA compared to total fluorescence yield (TFY) results, and shows significant suppression of the Zn K-shell lifetime broadening This result supports the use of asymmetric configurations for HERFD and XES at synchrotron light sources. The addition of 'clock angle' degrees of freedom to the common designs for multi-SBCA arrays for HERFD[45,46] would therefore allow *hkl*-hopping with increased user convenience, i.e., when a single analyzer is favorable for all user-desired emission lines in a given study, jumping between the different energy ranges would not require changing the SBCA and retuning.

We now move to our last study, a demonstration of XRS with an SBCA in an asymmetric configuration. Here we again used the Si(211) analyzer asymmetrically accessing the $\mathbf{G}_{hkl}$ = (642) reflection, approximately satisfying the condition $\theta_\mathrm{B} + \alpha = \theta_\mathrm{M} = 90$ deg at 8702.9 eV. The elastic line, measured by scanning the Si(111) double crystal monochromator, is shown in Fig. 16. The shape and (near) symmetry of the elastic peak illustrates a favorable energy response function for the experimental realization. The FWHM is 1.25 eV, which is comparable to the expected resolution of the Si(111) double crystal monochromator without second-crystal detuning, i.e., the analyzer is adding little broadening in this configuration. In addition, the source/sample-detector chord length of ~150 mm is quite large compared to that for synchrotron XRS spectrometers. This is beneficial due to the easier rejection of stray scatter and the larger

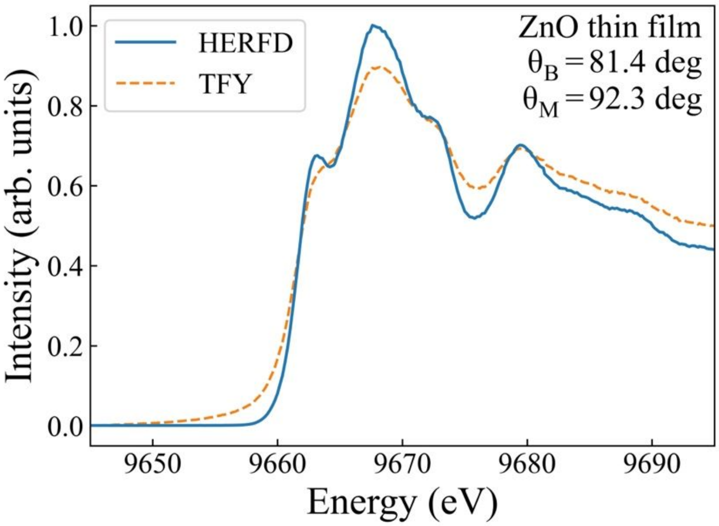

Figure 15: Zn HERFD-XANES measured with $\mathbf{G}_{hkl}$ = (642) of a Si(211) SBCA.

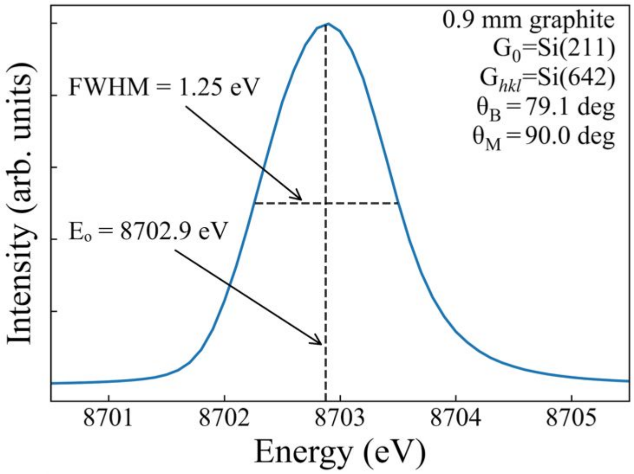

Figure 16: Elastic lines measured using a Si(211) analyzer asymmetrically $\mathbf{G}_{hkl}$ = (642), demonstrating Johann error elimination and narrowing of the analyzer response function when operated asymmetrically.

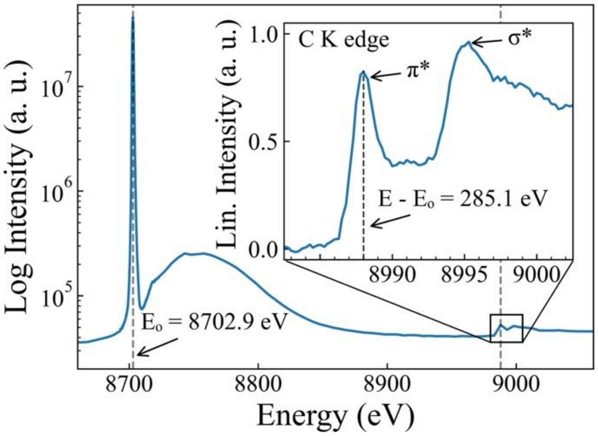

Figure 17: XRS of graphite showing elastic, inelastic, and XRS features of C K-edge. Measured with Si(211) using $\mathbf{G}_{hkl}$ = (642). The analyzer was mechanically at backscatter with a Bragg angle of 79.1 deg. The elastic peak FWHM is approximately 1.3 eV.

clearance for special sample environments. This configuration is best used with a focused beam to avoid source broadening, given the ~81 deg Bragg angle. We note that asymmetric operation of curved analyzers have been used before to accommodate unequal source-analyzer and analyzer-detector chords required by ancillary equipment.[35,47] However, here we make use of asymmetric operation to get high energy resolution and large analyzer solid angle together with good sample-to-detector clearance. Similar resolutions are reported in a prior XRS study using the von Hamos (non-Rowland) configuration[48], but it should be noted that contemporary XRS end stations overwhelmingly use arrays of SBCAs.[12,14,17,18] The resulting wide energy scan of the inelastic x-ray scattering and the C K-edge XRS itself are shown in Fig. 17, main panel and inset, respectively. The results indeed agree with the well-known spectrum for graphite. While these results are preliminary, they build on the strength of the prior demonstrations in this paper and strongly suggest the use of 0.5-m radius SBCA in XRS measurement, especially when a study requires focusing and thus makes source broadening irrelevant.

We note one detail missing from our present study: 0.5-m SBCA are typically sliced for strain relief which raises the question of whether the XRS imaging modality that is now is common use[49,50] may exhibit some degradation. This is an important topic for further study.

V. Conclusions

We investigate the merits of asymmetric Rowland geometries of spherically bent crystal analyzers (SBCAs) for laboratory based XAFS and XES as well as for synchrotron studies of high energy resolution fluorescence detection (HERFD) and x-ray Raman scattering (XRS). Several benefits of asymmetric operation are demonstrated. First, a single SBCA employed asymmetrically can use *hkl* hopping to access a large range of crystal planes and corresponding *d*-spacings, greatly extending the useful energy range with fine energy resolution compared to conventional symmetric operation. Second, by satisfying the condition that the source be at least relatively near to the SBCA sphere center, asymmetric Rowland geometries can mitigate or eliminate Johann error. Third, asymmetric Rowland geometries can significantly increase the clearance between sample and detector when the nominally perfect sphere-center geometry can be used. The combination of suppressed Johann error, larger solid angle (by use of the 0.5-m SBCA enabled by the elimination of Johann error), and large source-detector distance makes asymmetric operation an especially appealing paradigm for the design of future XRS endstations.

Acknowledgements

This work is supported by funding from the U.S. Department of Energy in the Nuclear Energy University Program under Contract No. DE-NE0009158. This research used resources of the Advanced Photon Source, a U.S. Department of Energy (DOE) Office of Science user facility operated for the DOE Office of Science by Argonne National Laboratory under Contract

No. DE-AC02-06CH11357. We thank each of Mali Balasubramanian and Pieter Glatzel for useful discussions, Shelly Kelly and Chengjun Sun for beamline assistance, and Abdullah Ceylan and Abdul Rumaiz for providing the thin film sample studied by HERFD XAS.

Bibliography

1 H. H. Johann, *Z. Für Phys.*, 1931, **69**, 185–206.
2 W. M. Holden, O. R. Hoidn, A. S. Ditter, G. T. Seidler, J. Kas, J. L. Stein, B. M. Cossairt, S. A. Kozimor, J. Guo, Y. Ye, M. A. Marcus and S. Fakra, *Rev. Sci. Instrum.*, 2017, **88**, 073904.
3 G. T. Seidler, D. R. Mortensen, A. J. Remesnik, J. I. Pacold, N. A. Ball, N. Barry, M. Styczinski and O. R. Hoidn, *Rev. Sci. Instrum.*, 2014, **85**, 113906.
4 G. T. Seidler, D. R. Mortensen, A. S. Ditter, N. A. Ball and A. J. Remesnik, *J. Phys. Conf. Ser.*, 2016, **712**, 012015.
5 M. E. Mundy, D. Ung, N. L. Lai, E. P. Jahrman, G. T. Seidler and B. M. Cossairt, *Chem. Mater.*, 2018, **30**, 5373–5379.
6 E. P. Jahrman, W. M. Holden, A. S. Ditter, D. R. Mortensen, G. T. Seidler, T. T. Fister, S. A. Kozimor, L. F. J. Piper, J. Rana, N. C. Hyatt and M. C. Stennett, *Rev. Sci. Instrum.*, 2019, **90**, 024106.
7 D. R. Mortensen, G. T. Seidler, J. J. Kas, N. Govind, C. P. Schwartz, S. Pemmaraju and D. G. Prendergast, *Phys. Rev. B*, 2017, **96**, 125136.
8 D. R. Mortensen, G. T. Seidler, A. S. Ditter and P. Glatzel, *J. Phys. Conf. Ser.*, 2016, **712**, 012036.
9 R. A. Valenza, E. P. Jahrman, J. J. Kas and G. T. Seidler, *Phys. Rev. A*, 2017, **96**, 032504.
10 W. M. Holden, G. T. Seidler and S. Cheah, *J. Phys. Chem. A*, 2018, **122**, 5153–5161.
11 D. Sokaras, D. Nordlund, T.-C. Weng, R. A. Mori, P. Velikov, D. Wenger, A. Garachtchenko, M. George, V. Borzenets, B. Johnson, Q. Qian, T. Rabedeau and U. Bergmann, *Rev. Sci. Instrum.*, 2012, **83**, 043112.
12 M. Moretti Sala, K. Martel, C. Henriquet, A. Al Zein, L. Simonelli, C. Sahle, H. Gonzalez, M.-C. Lagier, C. Ponchut, S. Huotari, R. Verbeni, M. Krisch and G. Monaco, *J. Synchrotron Radiat.*, 2018, **25**, 580–591.
13 S. Huotari, C. J. Sahle, C. Henriquet, A. Al-Zein, K. Martel, L. Simonelli, R. Verbeni, H. Gonzalez, M.-C. Lagier, C. Ponchut, M. Moretti Sala, M. Krisch and G. Monaco, *J. Synchrotron Radiat.*, 2017, **24**, 521–530.
14 D. Sokaras, T.-C. Weng, D. Nordlund, R. Alonso-Mori, P. Velikov, D. Wenger, A. Garachtchenko, M. George, V. Borzenets, B. Johnson, T. Rabedeau and U. Bergmann, *Rev. Sci. Instrum.*, 2013, **84**, 053102.
15 E. Kleymenov, J. A. van Bokhoven, C. David, P. Glatzel, M. Janousch, R. Alonso-Mori, M. Studer, M. Willimann, A. Bergamaschi, B. Henrich and M. Nachtegaal, *Rev. Sci. Instrum.*, 2011, **82**, 065107.
16 I. Llorens, E. Lahera, W. Delnet, O. Proux, A. Braillard, J.-L. Hazemann, A. Prat, D. Testemale, Q. Dermigny, F. Gelebart, M. Morand, A. Shukla, N. Bardou, O. Ulrich, S. Arnaud, J.-F. Berar, N. Boudet, B. Caillot, P. Chaurand, J. Rose, E. Doelsch, P. Martin and P. L. Solari, *Rev. Sci. Instrum.*, 2012, **83**, 063104.

17 T. T. Fister, G. T. Seidler, L. Wharton, A. R. Battle, T. B. Ellis, J. O. Cross, A. T. Macrander, W. T. Elam, T. A. Tyson and Q. Qian, *Rev. Sci. Instrum.*, 2006, **77**, 063901.

18 R. Verbeni, T. Pylkkänen, S. Huotari, L. Simonelli, G. Vankó, K. Martel, C. Henriquet and G. Monaco, *J. Synchrotron Radiat.*, 2009, **16**, 469–476.

19 J. F. Seely, E. Galtier, L. T. Hudson, A. Henins and U. Feldman, *Appl. Opt.*, 2019, **58**, 5225–5232.

20 A. Bordage, M. Pápai, N. S. Sas, J. Szlachetko, M. Nachtegaal and G. Vankó, *Phys. Chem. Chem. Phys.*, 2013, **15**, 11088–11098.

21 P. Suortti, T. Buslaps, P. Fajardo, V. Honkimäki, M. Kretzschmer, U. Lienert, J. E. McCarthy, M. Renier, A. Shukla, T. Tschentscher and T. Meinander, *J. Synchrotron Radiat.*, 1999, **6**, 69–80.

22 P. Suortti, U. Lienert and C. Schulze, *Nucl. Instrum. Methods Phys. Res. Sect. Accel. Spectrometers Detect. Assoc. Equip.*, 1994, **338**, 27–32.

23 L. Simonelli, C. Marini, L. Ribo, R. Homs, J. Avila, D. Heinis, I. Preda and K. Klementiev, *J. Synchrotron Radiat.*, 2023, **30**, 235–241.

24 P. Suortti and W. Thomlinson, *Nucl. Instrum. Methods Phys. Res. Sect. Accel. Spectrometers Detect. Assoc. Equip.*, 1988, **269**, 639–648.

25 P. Suortti, P. Pattison and W. Weyrich, *J. Appl. Crystallogr.*, 1986, **19**, 336–342.

26 P. Suortti, P. Pattison and W. Weyrich, *J. Appl. Crystallogr.*, 1986, **19**, 343–352.

27 P. Pattison, P. Suortti and W. Weyrich, *J. Appl. Crystallogr.*, 1986, **19**, 353–363.

28 P. Suortti, U. Lienert and C. Schulze, *AIP Conf. Proc.*, 1997, **389**, 175–192.

29 P. Suortti, D. Chapman, J. R. Schneider and T. Tschentscher, *J. Appl. Crystallogr.*, 1992, **25**, 432–438.

30 E. Erola, V. Eteläniemi, P. Suortti, P. Pattison and W. Thomlinson, *J. Appl. Crystallogr.*, 1990, **23**, 35–42.

31 T. Matsushita and U. Kaminaga, *J. Appl. Crystallogr.*, 1980, **13**, 465–471.

32 A. Boeuf, S. Lagomarsino, S. Mazkedian, S. Melone, P. Puliti and F. Rustichelli, *J. Appl. Crystallogr.*, 1978, **11**, 442–449.

33 R. Caciuffo, S. Melone, F. Rustichelli and A. Boeuf, *Phys. Rep.*, 1987, **152**, 1–71.

34 S. G. Podorov, O. Renner, O. Wehrhan and E. Förster, *J. Phys. Appl. Phys.*, 2001, **34**, 2363.

35 R. Bartiromo, F. Bombarda and R. Giannella, *Nucl. Instrum. Methods Phys. Res.*, 1984, **221**, 453–459.

36 M. Moretti Sala, K. Martel, C. Henriquet, A. Al Zein, L. Simonelli, C. Sahle, H. Gonzalez, M.-C. Lagier, C. Ponchut, S. Huotari, R. Verbeni, M. Krisch and G. Monaco, *J. Synchrotron Radiat.*, 2018, **25**, 580–591.

37 D. Sokaras, D. Nordlund, T.-C. Weng, R. A. Mori, P. Velikov, D. Wenger, A. Garachtchenko, M. George, V. Borzenets, B. Johnson, Q. Qian, T. Rabedeau and U. Bergmann, *Rev. Sci. Instrum.*, 2012, **83**, 043112.

38 D. Sokaras, T.-C. Weng, D. Nordlund, R. Alonso-Mori, P. Velikov, D. Wenger, A. Garachtchenko, M. George, V. Borzenets, B. Johnson, T. Rabedeau and U. Bergmann, *Rev. Sci. Instrum.*, 2013, **84**, 053102.

39 Y. M. Xiao, P. Chow, G. Boman, L. G. Bai, E. Rod, A. Bommannavar, C. Kenney-Benson, S. Sinogeikin and G. Y. Shen, *Rev. Sci. Instrum.*, 2015, **86**, 072206.

40 Y. Q. Cai, P. Chow, C. C. Chen, H. Ishii, K. L. Tsang, C. C. Kao, K. S. Liang and C. T. Chen, *AIP Conf. Proc.*, 2004, **705**, 340–343.

41 J. M. Ablett, D. Prieur, D. Céolin, B. Lassalle-Kaiser, B. Lebert, M. Sauvage, T. Moreno, S. Bac, V. Balédent, A. Ovono, M. M, F. Gélebart, A. Shukla and J.-P. Rueff, *J. Synchrotron Radiat.*, 2019, **26**, 263–271.

42 D. R. Mortensen and G. T. Seidler, *J. Electron Spectrosc. Relat. Phenom.*, 2017, **215**, 8–15.

43 K. Klementiev and R. Chernikov, in *Advances in Computational Methods for X-Ray Optics III*, SPIE, 2014, vol. 9209, pp. 60–75.

44 A. Ceylan, A. K. Rumaiz, D. Caliskan, S. Ozcan, E. Ozbay and J. C. Woicik, *J. Appl. Phys.*, 2015, **117**, 105303.

45 N. P. Edwards, J. R. Bargar, D. van Campen, A. van Veelen, D. Sokaras, U. Bergmann and S. M. Webb, *Rev. Sci. Instrum.*, 2022, **93**, 083101.

46 P. Glatzel, A. Harris, P. Marion, M. Sikora, T.-C. Weng, C. Guilloud, S. Lafuerza, M. Rovezzi, B. Detlefs and L. Ducotté, *J. Synchrotron Radiat.*, 2021, **28**, 362–371.

47 P. Jagodziński, D. Banaś, M. Pajek, A. Kubala-Kukuś, Ł. Jabłoński, I. Stabrawa, K. Szary, D. Sobota, A. Warczak, A. Gumberidze, H. F. Beyer, M. Lestinsky, G. Weber, T. Stöhlker and M. Trassinelli, *J. Instrum.*, 2023, **18**, P11002.

48 N. Watanabe, H. Hayashi, Y. Udagawa, K. Takeshita and H. Kawata, *Appl. Phys. Lett.*, 1996, **69**, 1370–1372.

49 C. J. Sahle, A. D. Rosa, M. Rossi, V. Cerantola, G. Spiekermann, S. Petitgirard, J. Jacobs, S. Huotari, M. Moretti Sala and A. Mirone, *J. Synchrotron Radiat.*, 2017, **24**, 269–275.

50 C. J. Sahle, A. Mirone, T. Vincent, A. Kallonen and S. Huotari, *J. Synchrotron Radiat.*, 2017, **24**, 476–481.